PAPER • OPEN ACCESS

MHD stability analysis against pressure and current-driven modes in the SMall Aspect Ratio Tokamak

OPEN ACCESS
IOP Publishing | International Atomic Energy Agency
Nuclear Fusion
Nucl. Fusion **64** (2024) 126028 (14pp)
https://doi.org/10.1088/1741-4326/ad7fd3

MHD stability analysis against pressure and current-driven modes in the SMall Aspect Ratio Tokamak

J. Dominguez-Palacios[1,2,9,*], M. Garcia-Munoz[1,2], M. Toscano-Jimenez[3], Y.Q. Liu[4], A. Mancini[1,2], D.J. Cruz-Zabala[1,2], J.W. Berkery[5], J.A. Labbate[6], J. Parisi[5], Y. Todo[7], A. Reyner-Viñolas[1,2], M. Podestà[5,10], E. Viezzer[1,2], P. Oyola[1,2] and S. Futatani[8]

[1] Department of Atomic, Molecular and Nuclear Physics, University of Seville, Avda. Reina Mercedes, Seville 41012, Spain
[2] Centro Nacional de Aceleradores, University of Seville, Junta de Andalucia CSIC, Avda. Thomas A. Edison 7, Seville 41092, Spain
[3] Department of Applied Physics III, University of Seville, Camino de los Descubrimientos s/n, Isla de la Cartuja, Seville 41092, Spain
[4] General Atomics, PO Box 85608, San Diego, CA 92186-5608, United States of America
[5] Princeton Plasma Physics Laboratory, Princeton, NJ, United States of America
[6] University of Maryland, College Park, WA D.C., United States of America
[7] National Institute for Fusion Science, National Institutes of Natural Sciences, Toki, Gifu 509-5292, Japan
[8] Universitat Politècnica de Catalunya, Barcelona, Spain

E-mail: jdominguezpalacios@us.es

Received 4 May 2024, revised 5 September 2024
Accepted for publication 25 September 2024
Published 8 October 2024

Abstract

Linear magnetohydrodynamic (MHD) simulations for the SMall Aspect Ratio Tokamak (SMART) have been carried out for the first time, for both positive (PT) and negative triangularity (NT) shaped plasmas using the MARS-F code. The MHD stability of projected SMART plasmas against internal kinks, infernal modes and edge peeling-ballooning modes have been analyzed for a wide range of realistic equilibria. A stabilization of internal kinks and infernal modes is observed when increasing the safety factor profile and reducing plasma beta. PT shaped plasmas are more stable against both internal kinks and infernal modes than their counterpart NT shaped plasmas. Toroidal flows have little impact on the MHD stability of the internal kinks, but they have a strong stabilizing effect on infernal modes, which can be further mitigated in NT shaped plasmas. The MHD stability of peeling-ballooning modes is reduced in NT shaped plasmas, as observed in conventional tokamaks.

Keywords: MHD, negative triangularity, SMART

(Some figures may appear in colour only in the online journal)

[9] Present address: Fiat Lux, San Diego, CA, United States of America.
[10] Present address: Ecole Polytechnique Fédérale de Lausanne, Swiss Plasma Center, CH-1015 Lausanne, Switzerland.
[*] Author to whom any correspondence should be addressed.

1. Introduction

Spherical tokamaks (STs) are a promising concept towards commercial fusion due to their compact form, cost-effectiveness and high power densities [1–3]. STs are characterized by having small aspect ratios, $A = R/a \lesssim 1.2-2.0$ (a, R are minor and major radius, respectively). Compared to the conventional high-aspect ratio ($A \gtrsim 3$) tokamaks, STs have shown high bootstrap current fractions [3, 4], improved stability against pressure-driven [2] and particle-driven instabilities [5, 6]. These benefits are generally attributed to enhanced plasma β ($\beta = p/B_0^2/2\mu_0$, i.e. ratio between kinetic and magnetic pressures) and, additionally, are thought to arise from the strong flow shear present in low aspect ratio plasmas [7, 8].

Not only low-aspect ratio plasmas show beneficial effects as those above mentioned, but the plasma shape is known to have a strong impact on the pressure and current limits [9, 10]. In conventional high-aspect ratio tokamaks, the effects of elongation and triangularity have been widely studied. Prior works showed that highly elongated and triangular plasmas have positive effects on the energy confinement time [11–13], electron heat transport [10], core stability [14] and edge stability in low and high confinement mode (L-mode and H-mode, respectively) plasmas [15, 16]. Negative Triangularity (NT) plasmas have shown H-mode plasma performance despite of being operated with L-mode-like edge pressure profiles, with low turbulence levels and a plasma edge devoid of Edge Localized modes (ELMs) [17–29], which supports the viability of an L-mode scenario for future fusion reactors [30].

Although NT high-aspect ratio plasmas have shown positive and encouraging results, little is known about the plasma shaping effects on plasma transport and stability in low-aspect ratio plasmas. The SMall Aspect Ratio Tokamak (SMART) [31–34] has been designed to study the prospects of non-conventional shaping, including NT for a ST based fusion power plant. Recently, reference scenarios for SMART [35] have been computed with the 1.5D transport code ASTRA [36] coupled with the equilibrium code FIESTA [37] to predict the temperature and density profiles, which are needed to foresee the expected SMART performance within basic magnetohydrodynamic (MHD) stability limits. A thorough MHD stability analysis, and its impact on the expected SMART operational regimes, has not been carried out yet.

This paper shows the first MHD stability analysis of projected SMART plasmas and is organized as follows. Section 2 presents the computational model employed to study the MHD stability of SMART. Section 3 shows the simulation results. Section 4 discusses the simulation results and their implications for the performance of SMART. The paper ends with the conclusions in section 5.

2. Computational models

In this work, the ideal MHD linear stability has been studied with the MARS-F code [38]. MARS-F solves the standard, linearized MHD equations in a generic toroidal geometry, and can include additional physical effects such as the toroidal equilibrium flow $\mathbf{V}_0 = R\Omega\mathbf{e}_\varphi$, where $\mathbf{V}_0$ is the flow velocity, Ω is the toroidal rotation angular frequency and $\mathbf{e}_\varphi$ is the unitary vector along the toroidal angle φ. The extended fluid equations including the toroidal equilibrium flow are shown below.

$$(\lambda + in\Omega)\,\rho_1 = -\nabla\cdot(\rho\mathbf{v}),$$
$$(\lambda + in\Omega)\,\boldsymbol{\xi} = \mathbf{v} + (\boldsymbol{\xi}\cdot\nabla\Omega)\,R^2\nabla\varphi, \tag{1}$$
$$\rho(\lambda + in\Omega)\,\mathbf{v} = -\nabla p + \mathbf{j}\times\mathbf{B} + \mathbf{J}\times\mathbf{Q} + \rho\left[2\Omega\nabla Z\times\mathbf{v} - (\mathbf{v}\cdot\nabla\Omega)\,R^2\nabla\varphi\right] \tag{2}$$
$$+\,\rho_1\Omega\nabla Z\times\mathbf{V}_0, \tag{3}$$
$$(\lambda + in\Omega)\,\mathbf{Q} = \nabla\times(\mathbf{v}\times\mathbf{B}) + (\mathbf{Q}\cdot\nabla\Omega)\,R^2\nabla\varphi, \tag{4}$$
$$(\lambda + in\Omega)\,p = -\mathbf{v}\cdot\nabla P - \Gamma P\nabla\cdot\mathbf{v}. \tag{5}$$

Here, ρ, $\mathbf{B}$, $\mathbf{J}$ and P are the equilibrium plasma density, magnetic field, plasma current density, and pressure, respectively. The perturbed quantities, which are related to the eigenfunction of the mode, are the perturbed plasma density ρ_1, the plasma displacement $\boldsymbol{\xi}$, the perturbed velocity $\mathbf{v}$, the perturbed magnetic field $\mathbf{Q}$, the perturbed plasma current density $\mathbf{j} = \nabla\times\mathbf{Q}$ and the perturbed plasma pressure p. The eigenvalue is λ and, generally, is a complex number (we use i to denote the imaginary unit); $\lambda = \gamma + i\omega$, where γ is the growth rate and ω is the mode frequency. The toroidal mode number is denoted by n, which will take the values $n = 1, \cdots, 10$. Finally, $\Gamma = 5/3$ is the ratio between the specific heats for the MHD closure. MARS-F solves the one-fluid MHD equations in a magnetic flux coordinate system (s, χ, φ), with $s \equiv \rho_{\rm pol} = \sqrt{(\Psi - \Psi_0)/(\Psi_{\rm LCFS} - \Psi_0)}$ the normalized poloidal flux coordinate [here, Ψ is the poloidal flux; Ψ_0 and $\Psi_{\rm LCFS}$ denote the poloidal flux at the magnetic axis and at the Last Closed Flux Surface (LCFS), respectively], χ is a generalized poloidal angle and φ denotes the toroidal angle. The grid resolution is $N_s \times N_\chi = 240 \times 960$.

The reference scenarios computed with ASTRA [35] are the Ohmic Baseline Scenario (OBS) and the Neutral Beam Injection Heated Scenario (NBIHS). In the NBIHS, the injection power is $P_{\rm NBI} = 1\,$MW and the injection energy is $E_{\rm NBI} = 25\,$keV. In these scenarios, the toroidal magnetic field, plasma current, elongation, triangularity, major radius and minor radius are $B_{\rm t} \sim 0.4\,$T, $I_{\rm p} \sim 0.2\,$MA, $\kappa \sim 1.95$, $\delta \sim 0.35$, $R_0 \sim 0.526\,$m and $a \sim 0.265\,$m, respectively. The normalized plasma beta, defined as $\beta_{\rm N} = \beta\,(\%) \times a\,({\rm m}) \times B_{\rm t}\,({\rm T})/I_{\rm p}\,({\rm MA})$[39, 40], is $\beta_{\rm N} \sim 1.4$ (~ 4.4) in the OBS (NBIHS). Both scenarios are characterized by a monotonically increasing safety factor profile q which we note has $q_0 < 1$, q_0 being the value at the magnetic axis. Figure 1 shows the thermal plasma profiles for the OBS and NBIHS, together with the safety factor profile. To scan the effects of the triangularity δ, we prescribe the plasma boundary using the following formula,

$$R = R_0 + a\cos(\theta + \delta\sin\theta), \tag{6}$$
$$Z = a\kappa\sin\theta, \tag{7}$$

where θ is the geometric poloidal angle. To obtain the MHD stability limits of SMART, the fixed boundary Grad-Shafranov

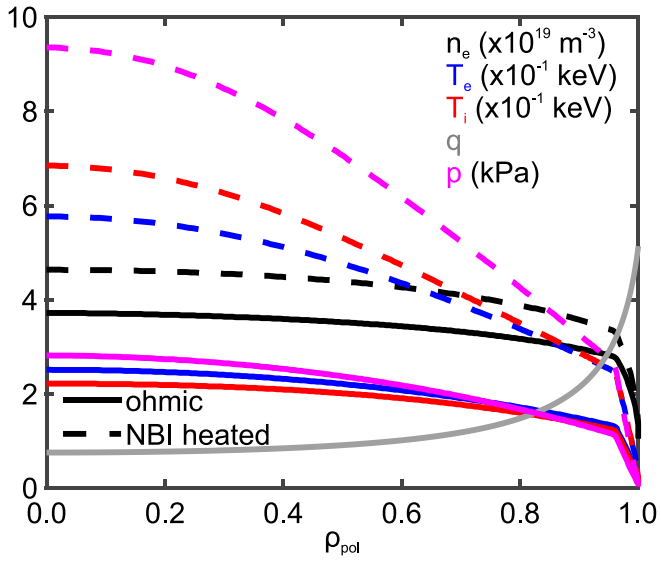

Figure 1. Electron density (black), electron temperature (blue), ion temperature (red), safety factor profiles (grey) and pressure (magenta) for the OBS (continuous) and NBIHS (dashed).

Table 1. Variables used throughout this paper and their normalization factors. Note that ω_A is the on-axis Alfvén frequency.

Symbol	Magnitude	Normalization
p	Pressure	B_0^2/μ_0
$I_\parallel$	Parallel current density	$B_0/(\mu_0 R_0)$
Ψ	Poloidal magnetic flux	B_0/R_0^2
γ	Linear growth rate	ω_A
ω	Frequency	ω_A

solver of CHEASE [41] is used to modify the equilibrium parameters. The elongation remains the same in all the equilibria examined in this work. Table 1 shows the normalization employed for the variables discussed in this work. Note that ω_A is the Alfvén frequency at the magnetic axis, $\omega_A = v_A/R_0$ and $v_A = B_0/\sqrt{\mu_0 m_H n_0}$ as we are studying a hydrogen plasma.

3. Simulation results

3.1. Core MHD stability

The ideal MHD stability analysis of SMART at the plasma core for the parameters of the OBS described above has been performed and is shown in this section. Figure 2 shows the linear growth rate of $n, = 1, \cdots, 10$ mode of the investigated scenario. The results indicate that the $n = 1$ internal kink [42–44] and the $n = 2, \cdots, 10$ (except $n = 3$) infernal modes [45, 46] are linearly unstable. The internal kink mode is an instability that takes place at the plasma core and is mostly driven by the plasma current. However, in tokamak plasmas, the internal kink is partly driven by the plasma pressure, in virtue of the Bussac criterion [43]. Infernal modes can be considered MHD instabilities driven both by the plasma pressure and plasma current, whose resonant surface is inside the plasma in a region where the magnetic shear is low and the

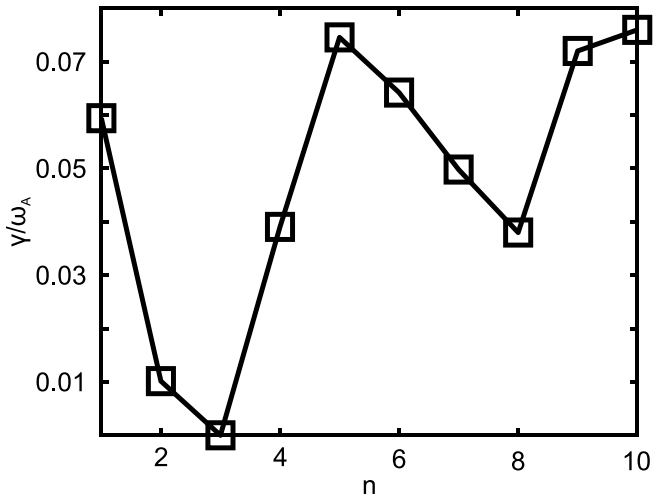

Figure 2. Linear growth rate of internal kink ($n = 1$) and infernal modes ($n = 2, \cdots, 10$) in the OBS case.

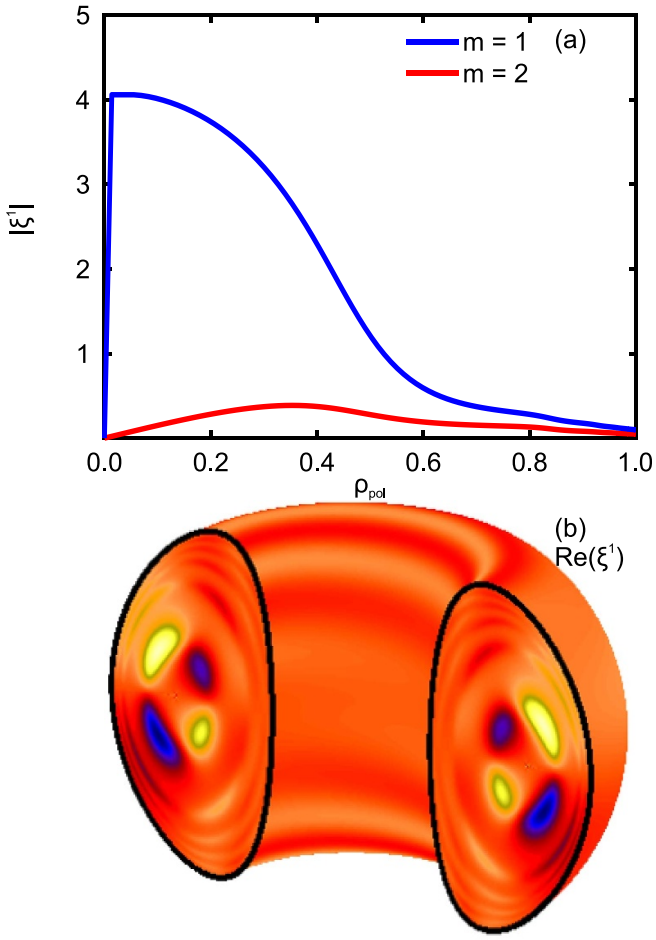

Figure 3. Spatial structure of $n = 1$ internal kink. (a) Radial profile, (b) 3D reconstruction. Black contours show the LCFS.

pressure gradient is large around the resonant surface, so that the pressure and current gradients drive are enough to compensate the stabilizing effect of the field-line bending [46, 47]. Figure 3(a) shows the radial profile of the $n = 1$ internal kink, together with a 3D reconstruction in figure 3(b). The

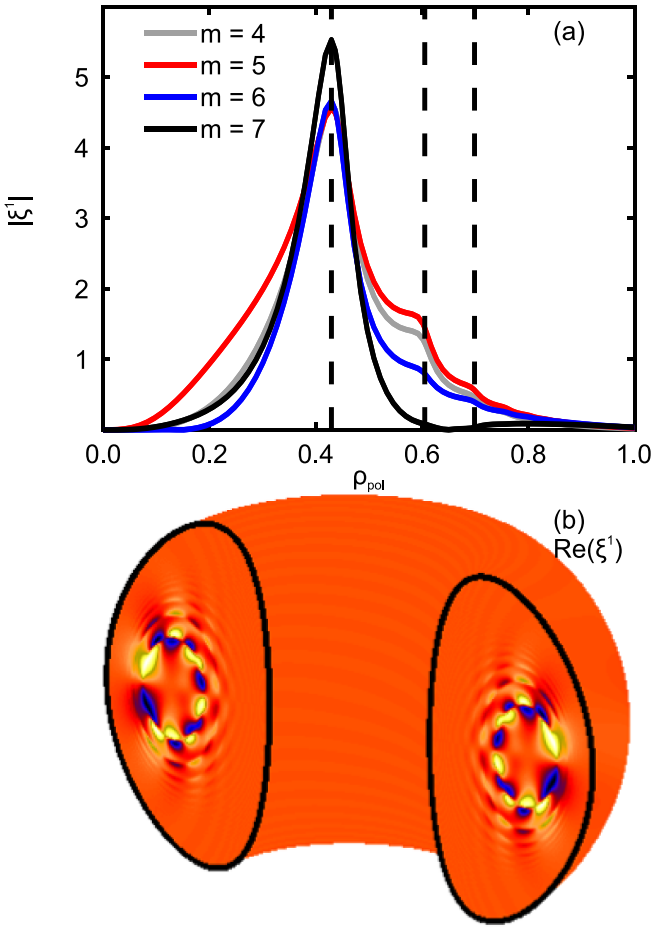

Figure 4. Spatial structure of $n = 5$ infernal mode. (a) Radial profile, (b) 3D reconstruction. Black contours show the LCFS. From left to right, the black vertical dashed lines represent the resonant surfaces $q_r = m/n = 1.0, 1.2, 1.4$, respectively.

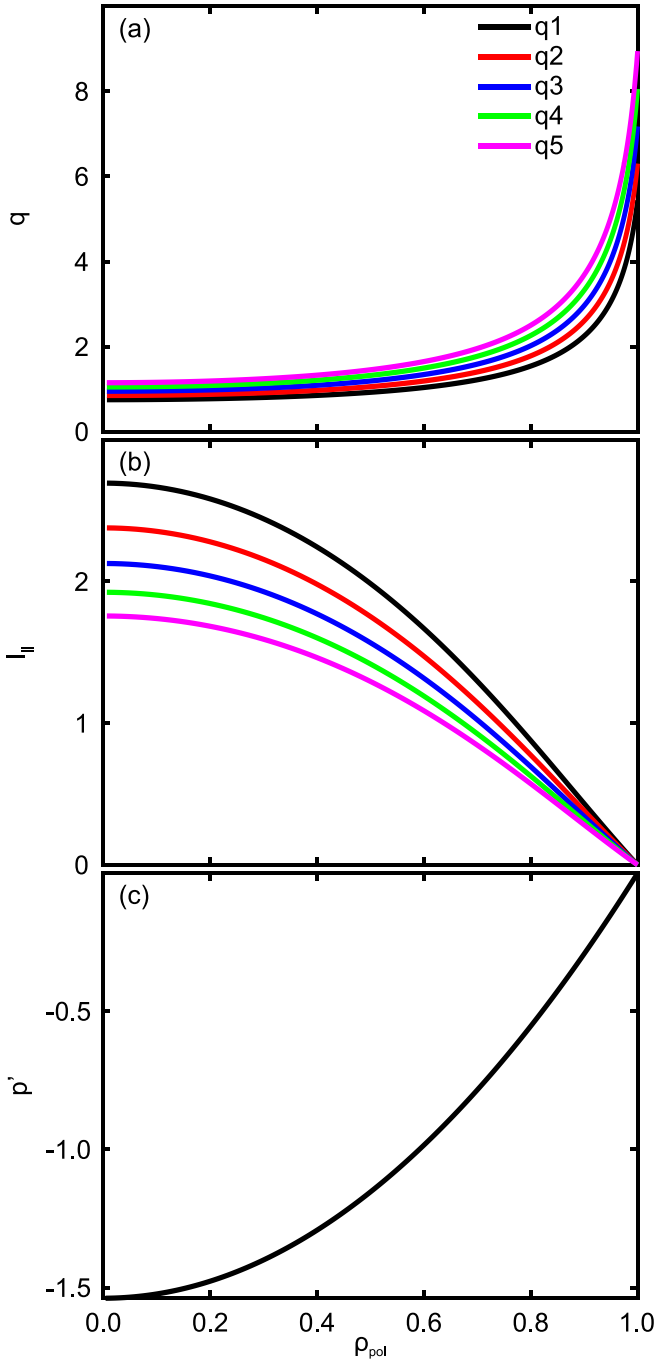

Figure 5. (a) q-profile, (b) normalized $I_{\|}$ and (c) p' profile during q_0 scan.

internal kink has a strong $(m,n) = (1,1)$ component, as well as a weak $(2,1)$ component. As an example of an infernal mode, figure 4(a) shows the radial profile of the $n = 5$ infernal mode, accompanied with its 3D reconstruction in figure 4(b). Infernal modes typically take place near $q = m/n \approx 1$ and when q is rather flat, which is the case under consideration. Both figures show $\left|\xi^1\right|$, where $\xi^1 = J\boldsymbol{\xi} \cdot \nabla\rho_{\text{pol}}$, and J is the Jacobian, $J = [\nabla\rho_{\text{pol}} \times (\nabla\chi \times \nabla\varphi)]^{-1}$.

In the following, parameter scans are carried out to understand the MHD stability limits of these modes, using a modified OBS equilibrium (unless otherwise specified) in which β_N is increased to $\beta_N = 2.2$ to make the $n = 3$ mode unstable and study its stability limits. We use the CHEASE code to prepare all these equilibria. CHEASE uses $I_{\|}$ and p' (or, equivalently, $\mathrm{d}p/\mathrm{d}\Psi$) profiles as input. The increase of β_N is achieved by multiplying p' profile by a constant. Additionally, we will remove any features at the plasma edge from $I_{\|}$ and p' profiles by making both of them go to zero. This is done to guarantee that peeling-ballooning modes are not simulated when other quantities such as β_N are scanned, since this section is focused on the MHD stability in the plasma core. To clarify the starting point for the parameter scans, tables will be included alongside the corresponding section if needed. The equilibrium mass density profile is given by $\rho = m_H n_e$. The equilibrium electron density profile, n_e, used in all the simulations always corresponds to that of the OBS to simplify our analysis.

3.1.1. Safety factor profile scan The effects of the safety factor profile are now addressed. Figure 5(a) shows the different q profiles used for the scan. These profiles are constructed by increasing q_0 by steps of 0.1. As the equilibria

Table 2. Reference values for equilibrium parameters used in the safety factor profile scan, see section 3.1.1.

Equation parameter	Value
δ	0.35
I_p	0.20 MA
q_0	0.75
q_a	5.44
β_N	2.20, 1.40

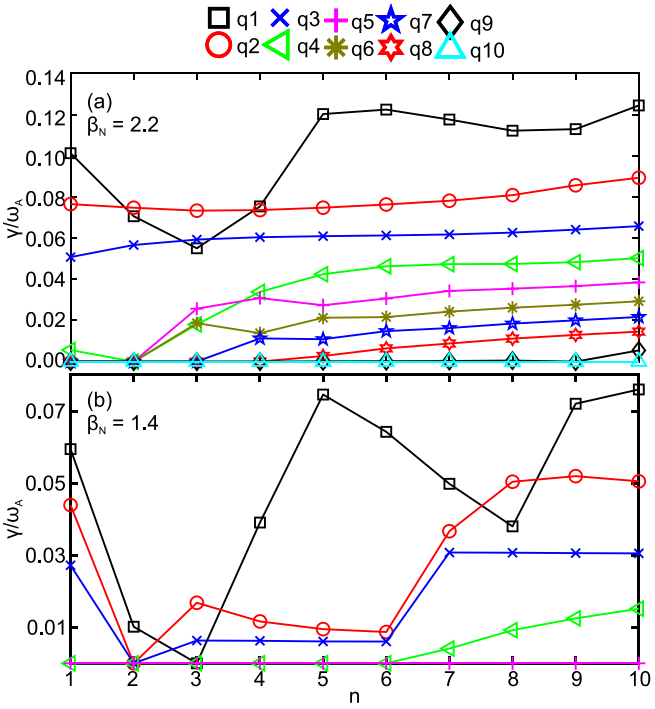

Figure 6. Linear growth rate γ vs toroidal mode number for each q profile for $\beta_N = 2.2$ (a) and $\beta_N = 1.4$ (b).

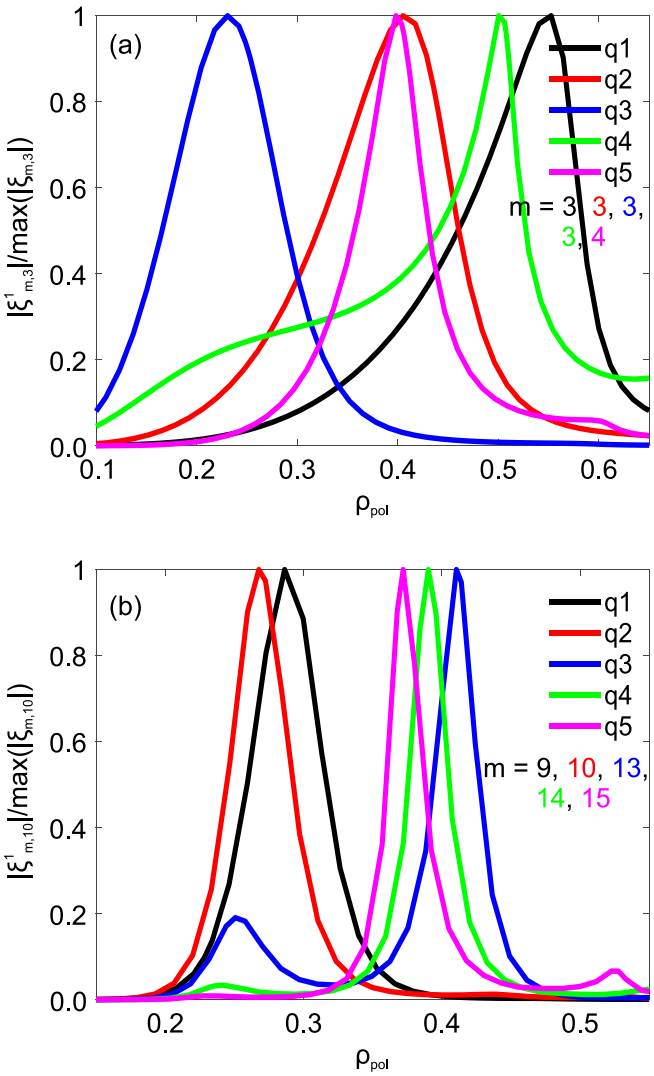

Figure 7. Radial profile for $n = 3$ (a) and $n = 10$ (b) modes for some of the q profiles scanned with $\beta_N = 2.2$. Only most unstable m poloidal mode number is shown for each case.

are calculated self-consistently for each case, a change in the q-profile also implies a change in the current density profile, as shown in figure 5(b). The p' profile does not change when modifying q during this scan and is shown in figure 5(c). We start from $q_0 = 0.75$, which corresponds to the case labeled as 'q1' and represents the starting point for this scan (the reference parameters are listed in table 2), and the case labeled as 'q10' has $q_0 = 1.65$. The current density and q profiles for 'q1' case are those of the original OBS.

The MHD stability of these equilibria are calculated and the linear growth rate for each toroidal mode is shown in figure 6 for $\beta_N = 2.2$ (a) and $\beta_N = 1.4$ (b). The linear growth rate of the $n = 1$ internal kink decreases for increasing q_0 and, for the 'q5' (a) ['q4' (b)]) case, it becomes stable. For $n \geqslant 4$ infernal modes, increasing q_0 has always a stabilizing effect as observed in figures 6(a) and (b), with the exception of $n = 8$ in figure 6(b) in the transition from 'q1' to 'q2'. In figure 6(a), the modes are stable for 'q10', whereas at $\beta_N = 1.4$ they are already stable in the 'q5' case. Note that $n = 2, 3$ modes become more unstable when q_0 increases from 'q1' to 'q2' in figure 6(a). Additionally, note that $n = 3$ mode is more unstable when q_0 increases from 'q4'to 'q5'. This can be understood if we examine how the mode profile changes with the q profile. Figures 7(a) and (b) show the $n = 3$ and $n = 10$ profiles for $\beta_N = 2.2$ and for several of the q profiles scanned. The different poloidal modes of $n = 3$ peak at q = 1.20 ('q1'), 0.97 ('q2'), 0.99 ('q3'), 1.32 ('q4') and 1.32 ('q5') for $m = 3, 3, 3, 3, 4$, respectively, whereas $n = 10$ peaks at q = 0.80 ('q1'), 0.9 ('q2'), 1.1 ('q3'), 1.2 ('q4') and 1.3 ('q5') for $m = 9, 10, 13, 14, 15$, respectively. With regards to $n = 3$, the mode is more unstable in 'q2' than in 'q1' because the $|\Delta q|$ decreases (here, $\Delta q = q_{peak} - q_r$, q_{peak} is the value of q at the peak location and $q_r = m/n$ is the value at the resonant surface), reducing the field-line bending stabilizing effect. From 'q2' to 'q3', the mode moves to an inner radial location where the current gradient drive at the resonant surface is smaller, reducing the drive and, therefore, reducing the growth rate. From 'q3' to 'q4', the mode moves to an outer radial location where $|\Delta q|$ increases, which increases the field-line bending stabilizing effect. Finally, at 'q5' we get a smaller $|\Delta q|$,

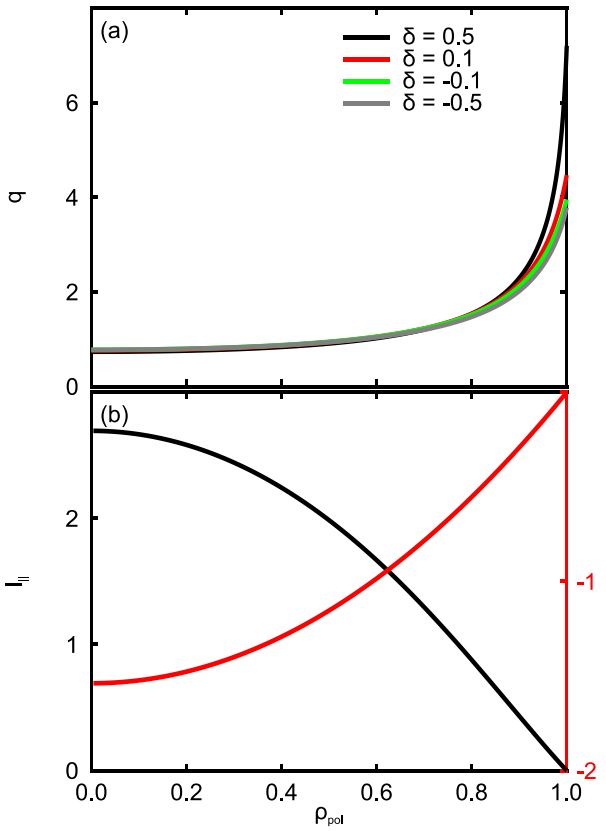

Figure 8. (a) Safety factor q profile for different triangularities. (b) Normalized $I_{\|}$ and p' profiles used for the δ scan.

and the mode peaks at an inner radial location, where the current gradient is smaller. For $n=10$, the field-line bending does not change so much between 'q1' and 'q2'. Additionally, the mode peaks at similar locations in both simulations, therefore the pressure and current gradient drives should be very similar. However, the unstable m increases from 9 to 10, and that could have a stabilizing effect, as the growth rate scales with $1/m^2$ [46, 48]. For the rest of cases, Δq takes similar values and m increases, which has a stabilizing effect.

3.1.2. Triangularity scan. We analyze now the MHD stability of the internal kink and infernal modes for several values of δ. Figure 8(a) shows the q-profile for the different δ values examined here. The q-profile is modified mostly at the edge of the plasma. In this scan, $I_{\|}$ and p' take the values of the modified OBS equilibrium with $\beta_N=2.2$, previously labelled as 'q1' in the q scan, and both go to zero at the plasma edge, as shown in figure 8(b). Table 3 summarizes the equilibrium parameters of the starting point of this scan. Figure 9 shows the linear growth rate of the $n=1$ internal kink and $n=2,\cdots,10$ infernal modes for each δ. In general, the decrease of the triangularity makes the plasma more linearly unstable against these modes, which suggests that the internal kink and infernal modes have a reduced MHD stability boundary in NT SMART plasmas.

We analyze the triangularity effects in more detail. Figure 10(a) shows $(m,n)=(4,5)$ mode profile for $\delta=\pm0.5$,

Table 3. Reference values for equilibrium parameters used in the triangularity scan, see section 3.1.2.

Equation parameter	Value
δ	-0.50
I_p	0.20 MA
q_0	0.75
q_a	3.78
β_N	2.80

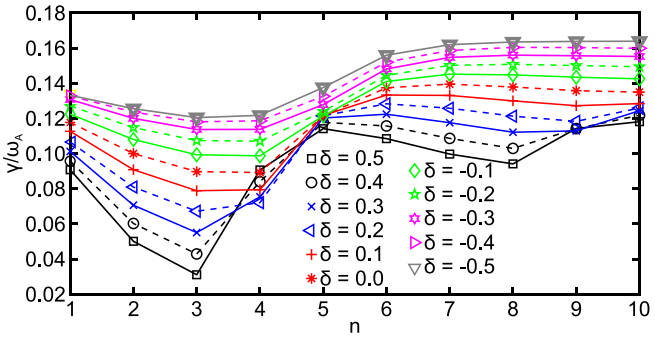

Figure 9. Linear growth rate of core $n=1,\cdots,10$ modes for different δ values.

which corresponds to the pair of modes (m,n) most unstable for $n=5$, peaking close to the resonant surface $q_r=0.8$. As we can observe, the mode moves radially inwards when $\delta=-0.5$, where the pressure is larger; note that the growth rate of infernal modes is proportional to β_p^2 [48]. This might explain the increasing growth rate for medium-n infernal modes.

For high-n infernal modes, we observe the opposite. In figure 10(b), we plot the $n=10$ mode profile for the most unstable m for both $\delta=\pm0.5$. In this case, the mode moves radially outwards when $\delta=-0.5$. The value of $\Delta q/q_r$ is very similar for both cases, and the pressure slightly decreases when the mode moves radially outwards. The most plausible explanation is found in the shape of each individual flux surface. The flux surfaces for both $\delta=\pm0.5$ are shown in figure 11. When approaching the plasma core, the triangularity of the flux surfaces tend to decrease. Therefore, the destabilizing effect of increased curvature brought by NT will become more pronounced for modes that are localized radially outwards. For $n=5$, the mode peaks at flux surfaces with similar shape. However, $n=10$ mode peaks at $\rho_{pol}\approx0.32$ (0.45) for $\delta=+(-)0.5$, therefore we might expect some additional destabilizing effect on the infernal mode. This could also explain why $n=1$ is more unstable in NT, as the internal kink can extend to $\rho_{pol}\approx0.5$ as shown in figure 3.

3.1.3. Plasma beta scan. We have analyzed the β_N limit of the SMART tokamak due to the internal kink and infernal modes. In the β_N scan, the q-profile slightly changes, as shown in figure 12(a). In this scan, we start from the modified OBS equilibrium labeled as 'q5' in figure 5 and table 4 summarizes the equilibrium parameters of such a case. Figure 12(b) shows the linear growth rate of the $n=1$ internal kink and

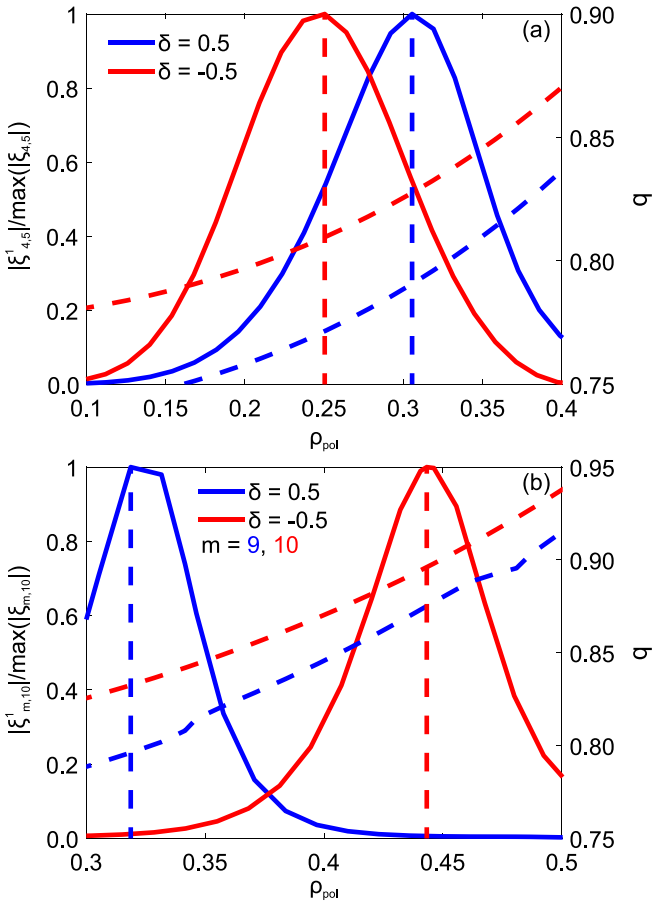

Figure 10. Mode $(m,n) = (4,5)$ (*a*) and mode $n = 10$ (*b*) profiles for $\delta = \pm 0.5$ (left axis, full line), safety factor (right axis, colored dashed lines). Colored vertical dashed lines are used to highlight the value of q at the corresponding mode peak location. Only most unstable poloidal mode numbers are shown for each case.

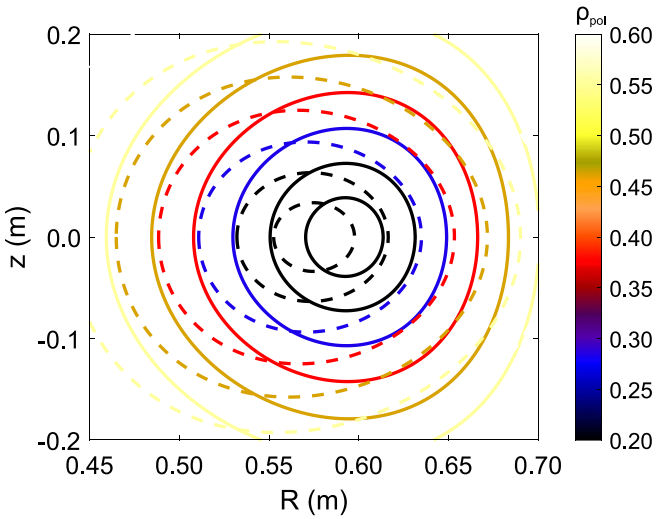

Figure 11. Flux surfaces labelled by $\rho_{\rm pol}$ in the poloidal plane zoomed at the plasma core, for $\delta = +0.5$ (dashed) and $\delta = -0.5$ (full).

$n = 2,\cdots,10$ infernal modes for several values of $\beta_{\rm N}$. It is observed that the infernal modes are linearly unstable from $\beta_{\rm N} \geqslant 2$. Notice that, according to the result shown in figure 12, $n = 1,\cdots,10$ modes will be linearly unstable in the NBIHS due to the larger $\beta_{\rm N}$ compared to the OBS.

3.1.4. Ideal MHD stability analysis with MEGA. The linear ideal MHD stability analysis of internal kink and infernal modes has also been performed using the MHD module of the MEGA code without non-ideal physical effects and without energetic particles [49]. We consider the equilibrium case with $\delta = -0.5$ shown in figures 8(*a*) and (*b*). The linear growth rate of $n = 1,\cdots,10$ modes calculated with MEGA and MARS-F is shown in figure 13. The largest relative difference between the growth rates obtained with both codes is 14%. The difference probably comes from the mapping of the equilibrium from the flux-coordinate system to the rectangular box of (R,z). Since the differences between MARS-F and MEGA simulation results are small, we conclude that both calculations reasonably agree.

3.2. Toroidal flow effects on internal kink and infernal modes

Toroidal rotation flow shall be considered in this subsection. For this study, we consider two different toroidal rotation frequency profiles, which is the input we give to MARS-F. The analytical formula we use to construct the toroidal angular rotation profile is

$$\frac{\Omega}{\omega_{\rm A}} = \frac{1}{2}\frac{\Omega_0}{\omega_{\rm A}}\left[1 - \tanh\left(\frac{\rho_{\rm pol} - \rho_0}{\sigma_\rho}\right)\right], \tag{8}$$

where ρ_0 and σ_ρ are the parameters we use to modify the flow shear, and $\frac{\Omega_0}{\omega_{\rm A}}$ controls the amplitude of the profile. Figure 14 shows two different profiles of the normalized toroidal rotation frequency profile, labelled as 'p1' and 'p2'. The parameters are

$$\text{p1}: \rho_0 = 0.45, \sigma_\rho = 0.1, \tag{9}$$
$$\text{p2}: \rho_0 = 0.15, \sigma_\rho = 0.3, \tag{10}$$

and, for both kind of profiles, we will consider different values of $\frac{\Omega_0}{\omega_{\rm A}}$. In this work, the equilibrium calculation ignores the toroidal flows. This assumption is reasonable, since the toroidal flows considered here are much smaller than the sound speed [50–53].

We study the effects of the toroidal rotation frequency in both positive and negative triangularities, taking $\delta = \pm 0.5$ examined previously in the triangularity scan. The maximum amplitude of rotation considered in this work are in the range of those observed in a MAST plasma discharge [54]. The rest of equilibrium profiles and parameters are taken from the modified OBS equilibrium with $\beta_{\rm N} = 2.2$ and $q_0 < 1$. Figures 15(*a*)–(*d*) show the linear growth rate of $n = 1,\cdots,10$ modes and figures 15(*e*)–(*h*) their frequency for $\delta = 0.5$ and $\delta = -0.5$, respectively. According to our simulation results, the effect of the toroidal rotation frequency on the linear growth rate can be stronger for $\delta = -0.5$ than for $\delta = 0.5$. One can see that, for the 'p1' rotation profile, the linear growth rate of the infernal modes $n \geqslant 5$ decreases faster in NT plasmas compared to Positive Triangularity (PT) plasmas. For

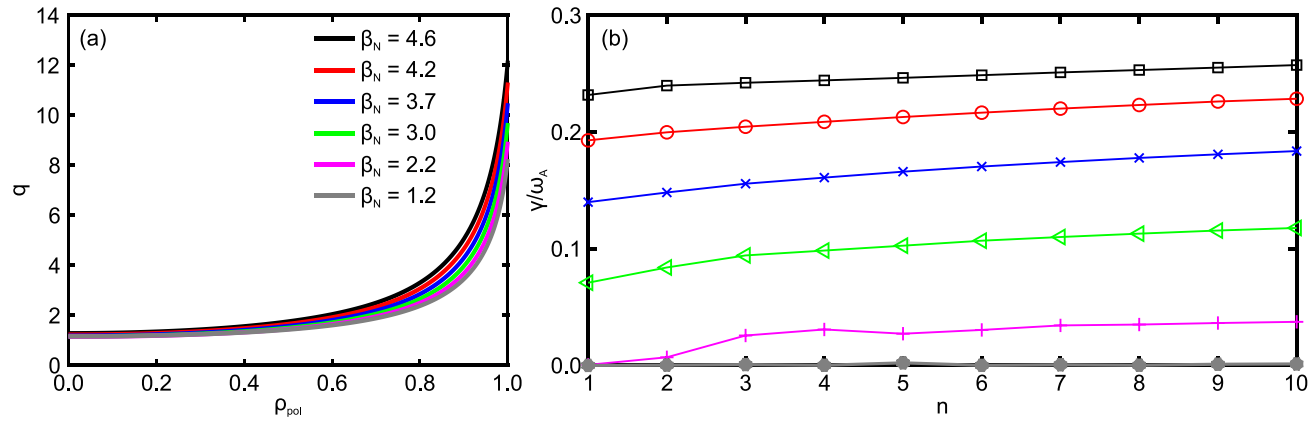

Figure 12. (*a*) q-profile for each β_N examined. (*b*) Linear growth rate for the $n = 1$ internal kink and $n = 2, \cdots, 10$ infernal modes for several values of β_N.

Table 4. Reference values for equilibrium parameters used in the plasma beta scan, see section 3.1.3.

Equation parameter	Value
δ	0.35
I_p	0.15 MA
q_0	1.15
q_a	8.95
β_N	4.60

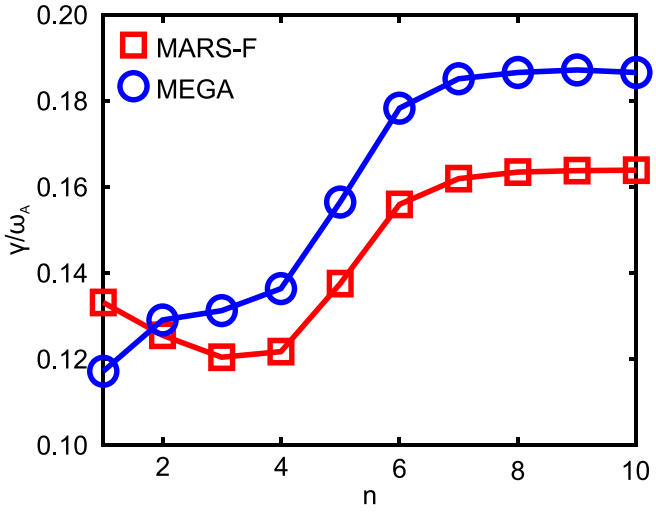

Figure 13. Linear growth rate of core $n = 1, \cdots, 10$ modes calculated with MEGA and MARS-F, for the $\delta = -0.5$ case.

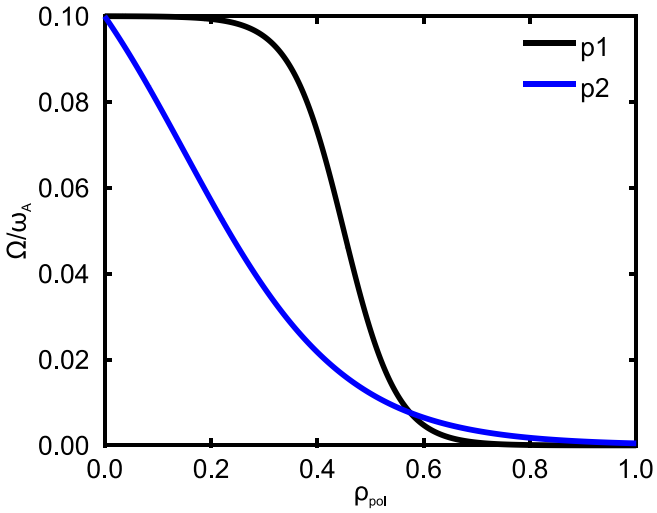

Figure 14. Toroidal rotation profiles normalized by ω_A for $\frac{\Omega_0}{\omega_A} = 0.10$.

instance, the highest linear growth rate observed in NT plasmas is reduced by a factor of 62.5%, whereas it is reduced by a factor of 16.7% in PT plasmas. This is expected since figure 10(*b*) shows where the high-n modes peak in PT and NT. The high-n infernal modes peak at the radial location where the flow gradient is large for the 'p1' case in NT, whereas in PT peak at an inner radial location, where the flow gradient is smaller. It can also be observed that the most unstable mode number, in the presence of toroidal flows, is $n = 1$ in NT plasmas, but higher-n modes still remain as the most unstable ones in PT plasmas. The 'p2' rotation profile, on the other hand, has a weaker effect on the mode stability. Notice that, for the 'p2' case, the impact on the $n = 4$ linear growth rate is stronger than that observed for the 'p1' case, while for $n = 3$ the observation is the opposite. It is also worth noting that the toroidal flow practically does not affect the linear growth rate of low-n modes ($n = 1, 2$), having a very weak destabilizing effect. Note that the frequency of the modes is affected in the presence of toroidal flows. We see that the modes have a larger frequency for the 'p1' rotation profile than for 'p2' case for both triangularities examined here. For high-n infernal modes, note that $\omega \sim n\Omega(\rho_{pol})$, however this does not hold for lower-n modes, as these are less localized. Note that $\Omega(\rho_{pol})$ corresponds to the local rotation frequency at the radial location of the mode.

Figure 16 shows a β_N scan with and without toroidal flows (the case with toroidal flows considers the 'p1' profile and $\Omega_0/\omega_A = 0.10$), for both $\delta = \pm 0.5$. In the ideal MHD simulation, the modes are always more unstable in NT. However, in the presence of toroidal flows, most of the infernal modes are completely suppressed at $\beta_N = 1.4$, which is the value

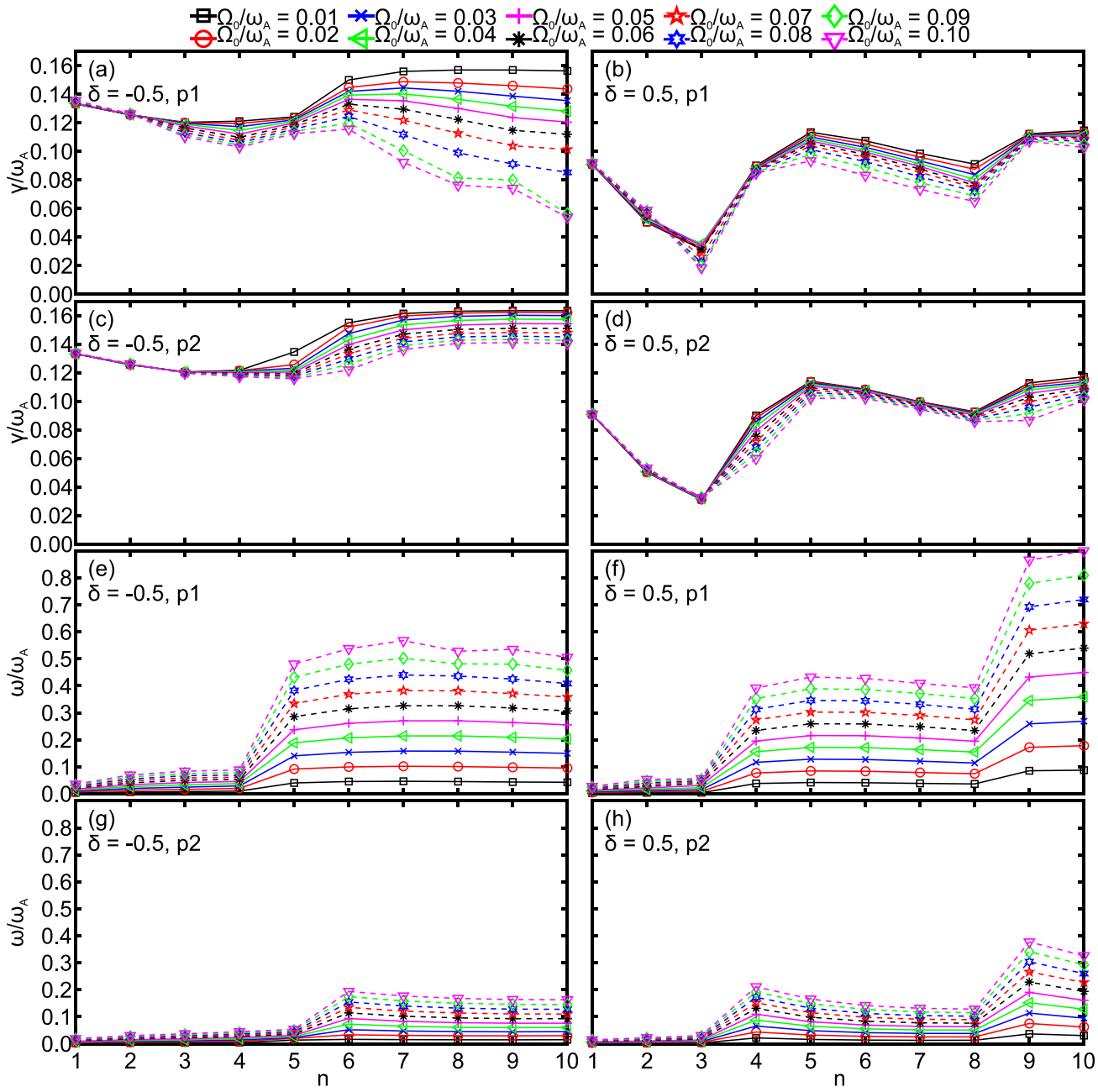

Figure 15. Linear growth rate (*a*)–(*d*) and frequency (*e*)–(*h*) of $n = 1, \cdots, 10$ modes in the presence of toroidal flows for $\delta = -0.5$ (left column) and $\delta = 0.5$ (right column). Panels (*a*) [(*c*)], (*b*) [(*d*)], (*e*) [(*g*)] and (*f*) [(*h*)] correspond to p1 (p2) case.

for the OBS, being $n = 2, 5, 6$ the infernal modes remaining unstable, with a larger growth rate than in the PT plasma.

3.3. MHD stability of peeling-ballooning modes

Peeling-ballooning modes are driven by the pressure gradients and current densities at the plasma edge and are thought to describe the ELM onset [55]. An example of such modes at the plasma edge of SMART is shown in figures 17(*a*)and (*b*), which depicts the 3D structure of $n = 10$ mode for $\delta = 0.5$ and $\delta = -0.5$, respectively. Here, we study how the peeling-ballooning MHD stability boundary of SMART is affected by the triangularity. A set of equilibria with different pressure gradient and current densities at the plasma edge are generated for different values of δ. The pressure gradient and current density are modified as follows,

$$p'_{\rm mod} = p'_{\rm old} - C_p \exp\left[-\left(\frac{\rho_{\rm pol} - \rho_0}{\sigma}\right)^2\right], \qquad (11)$$

$$I_{\parallel_{\rm mod}} = I_{\parallel_{\rm old}} + C_j \exp\left[-\left(\frac{\rho_{\rm pol} - \rho_0}{\sigma}\right)^2\right]. \qquad (12)$$

Here, the subindices 'mod' and 'old' stand for the modified profile and the profile without any feature at the edge,

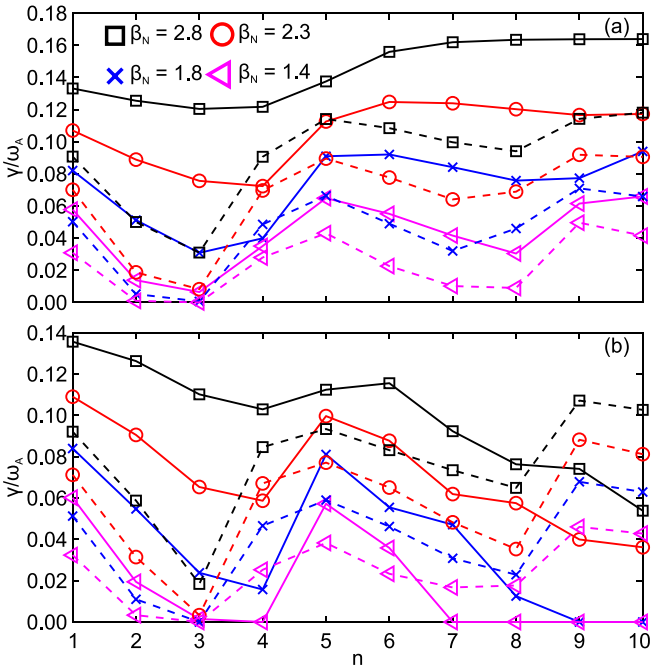

Figure 16. Plasma beta effects without (*a*) and with (*b*) toroidal flows, using 'p1' profile with $\Omega_0/\omega_A = 0.10$, for $\delta = -0.5$ (full) and $\delta = +0.5$ (dashed).

respectively, and $\rho_0 = 0.96$, $\sigma = 0.02$, thus the modification is directly applied at the plasma edge by creating a (C_p, C_j) matrix that ranges from $[(4-0),(0-3)]$. The 'old' p' and $I_\parallel$ profiles are those labelled as 'q1' in the safety factor profile scan shown in figure 5, and the equilibrium parameters used there (see table 2) correspond to the starting point of this study, except for the triangularity, as will be clarified shortly. The peeling-ballooning MHD stability diagram will be shown in $(\alpha_{\max}, j_{\text{ped}}/\langle j\rangle)$ coordinate space, since they are the drivers for the peeling-ballooning modes. They represent the normalized pressure gradient and current density, respectively, and are defined as [56, 57]

$$\alpha = \frac{\mu_0}{2\pi^2}\frac{\partial V}{\partial \Psi}\left(\frac{V}{2\pi^2 R}\right)^{0.5}\frac{\mathrm{d}p}{\mathrm{d}\Psi}, \alpha_{\max} = \max(\alpha), \tag{13}$$

$$\frac{j_{\text{ped}}}{\langle j\rangle} = \frac{\max\left(I_\parallel\right)}{\langle I_\parallel\rangle}, \tag{14}$$

where V is the volume of a flux surface and $\langle(\cdot)\rangle$ means average with respect to the poloidal flux of $(\cdot)$. Figures 18(*a*) and (*b*) represents the peeling-ballooning MHD stability diagram in SMART for triangularities $\delta = \pm 0.3$, respectively. The figure is colored according to the linear growth rate of the most unstable mode number at the corresponding grid point of the $(\alpha_{\max}, j_{\text{ped}}/\langle j\rangle)$ mesh. The dark regions correspond to grid points of the $(\alpha_{\max}, j_{\text{ped}}/\langle j\rangle)$ mesh in which no peeling-ballooning mode is observed to be linearly unstable. The simulation results indicate that NT plasmas are prone to be more limited by peeling-ballooning modes, since for $\delta = -0.3$ the stable region has a smaller area compared to plasmas with $\delta = 0.3$.

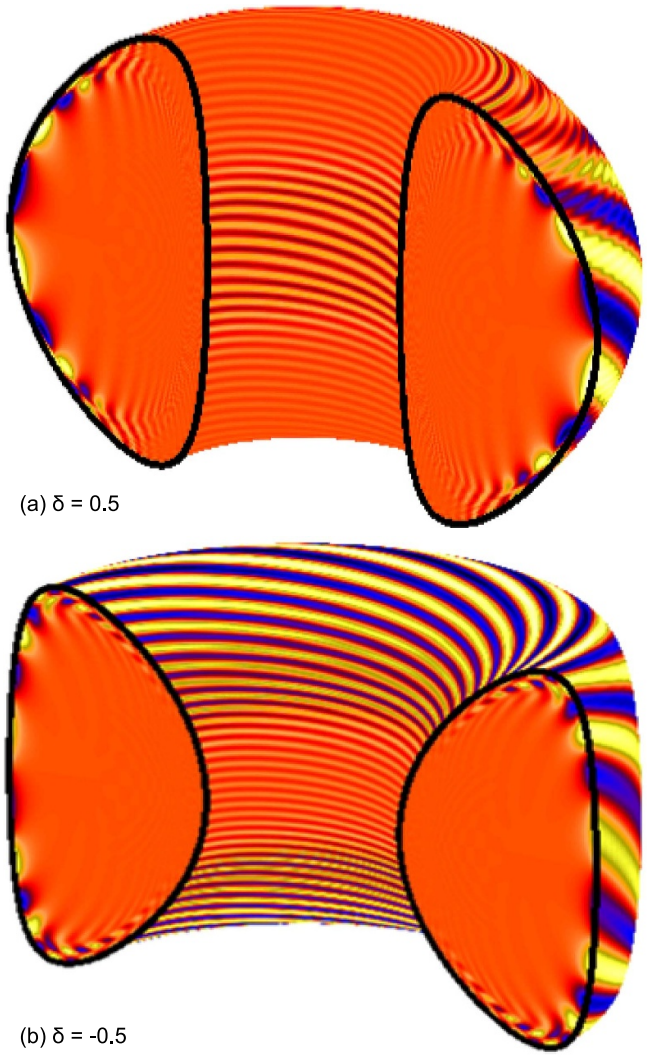

Figure 17. 3D illustration of an $n = 10$ mode at the edge of SMART for $\delta = 0.5$ (*a*) and $\delta = -0.5$ (*b*). Black contours show the LCFS.

In addition, we have computed the linear MHD stability diagram of peeling-ballooning modes for a configuration of SMART with higher aspect ratio. This will allow us to address the question of whether a conventional tokamak would show better MHD stability properties against peeling-ballooning modes compared to STs. The aspect ratio is increased to $A = 3$ by increasing R_0 while fixing a. The magnetic field has also been changed, so that the plasma beta and total current are as close as possible to the original spherical case. The matrix (C_p, C_j) ranges from $[(13-0),(0-5.5)]$ in this case. Figures 18(*c*) and (*d*) illustrates the MHD stability diagram for $\delta = 0.3$ and $\delta = -0.3$ with $A = 3$, respectively. For a plasma with aspect ratio $A = 3$, the plasma is more prone to develop peeling-ballooning modes compared to the spherical case. Notice that, for a conventional tokamak, the NT configuration also shows a reduced MHD stability boundary compared to its positive counterpart.

Additionally, we have performed a triangularity scan while fixing p' and $I_\parallel$ as observed in figure 19, which shows how the q, $I_\parallel$ and p' are taken for this scan. In such a case, $\alpha_{\max} \approx 12$

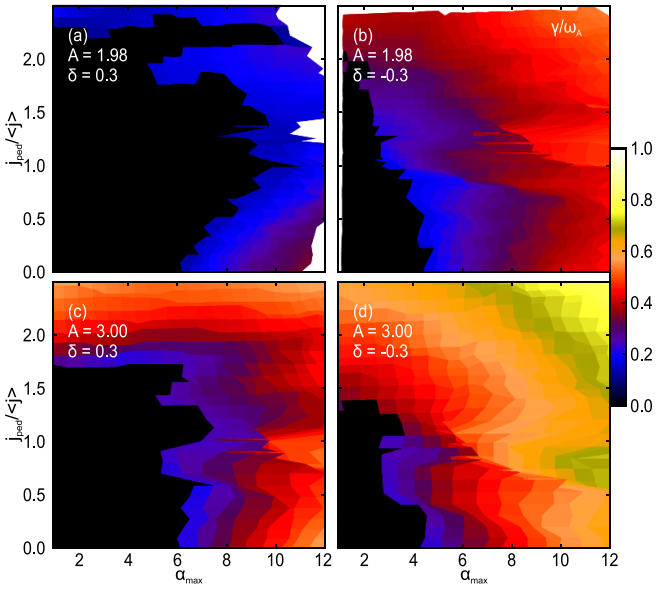

Figure 18. Peeling-ballooning MHD stability diagram for aspect ratio $A = 1.98$ (top row) and $A = 3$ (bottom row). In the figures, $\delta = 0.3$ (a), (c) and $\delta = -0.3$ (b), (d). The color corresponds to the linear growth rate of the most unstable mode number at the corresponding grid point of the $(\alpha_{\max}, j_{\rm ped}/\langle j\rangle)$ mesh.

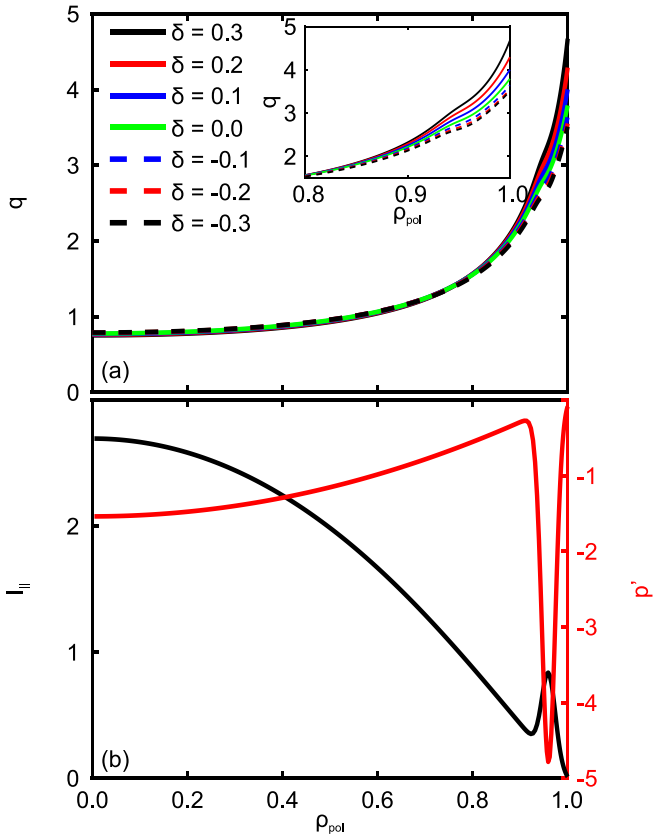

Figure 19. (a) q profile for the δ scan of peeling-ballooning modes. Inset shows a zoom in the pedestal region. (b) Normalized $I_{\|}$ and p' for the δ scan of peeling-ballooning modes.

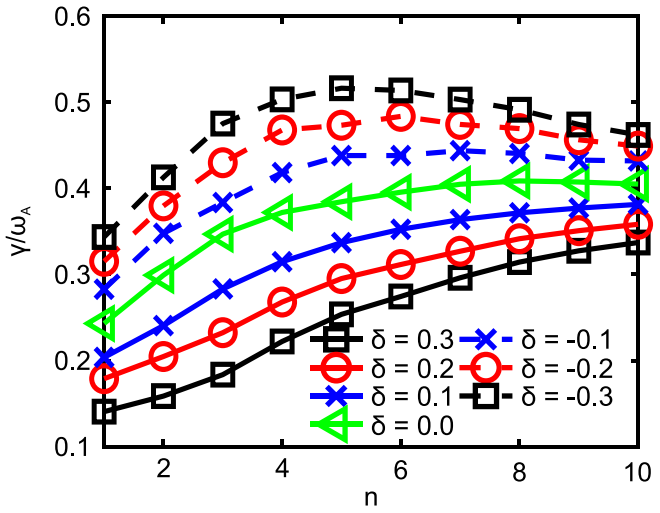

Figure 20. Linear growth rate of peeling-ballooning $n = 1, \cdots, 10$ modes for different δ.

and $j_{\rm ped}/\langle j\rangle \approx 1.8$, while q changes as a consequence of changing the triangularity, as observed in the inset of figure 19(a). Figure 20 depicts the simulation results for this scan, with a large pressure gradient at the edge, and we observe that the linear growth rate of finite-n peeling-ballooning modes is strongly impacted when the triangularity changes (this can also be inferred from figure 18). For lower triangularity, and especially for $\delta < 0$, we see that the linear growth rate of $n = 1, \cdots, 10$ increases. In addition, while keeping fixed $I_{\|}$ and p' during the scan, the most unstable mode number shifts to a lower one. As it can be observed, $n = 10$ is the most unstable mode for $\delta = 0.3$, whereas $n = 5$ becomes the most unstable one for $\delta = -0.3$. Therefore, changing the triangularity not only impacts the stability diagram for peeling-ballooning modes but can also shift the most unstable mode number.

The p' (and therefore α) for this scan is deliberately chosen to be large (well into the unstable region of figure 18) to test the behavior of unstable peeling-ballooning modes as plasma triangularity is modified. Infinite-n ballooning stability, calculated with the codes BALOO [58] and ballstab (a module of GS2 [59]), for the δ scan of figure 20, shows the expected behavior from reference [60], and consistent with figure 18, that when δ decreases the plasma is ballooning unstable for a wider range of α values. As shown in figure 21(a), the peak α is predicted to be in the second stability region, but there is no open window of stability in $(\alpha, \rho_{\rm pol})$ space to support the steep H-mode like pedestal assumed in figure 19, even at the highest triangularity. Figure 21(b) shows the ballstab calculation of s vs. $-{\rm d}\beta/{\rm d}(r/a)$ for four flux surfaces, where $s = (r/q)({\rm d}q/{\rm d}r)$ is the magnetic shear and $-{\rm d}\beta/{\rm d}(r/a)$ is a quantity similar to α. The figure confirms that flux surfaces interior to the peak p' are stable, around the peak p' are unstable, and at the peak are in the second stability region. However, the s value is too large for an open window to second stability which would allow this steep pressure profile.

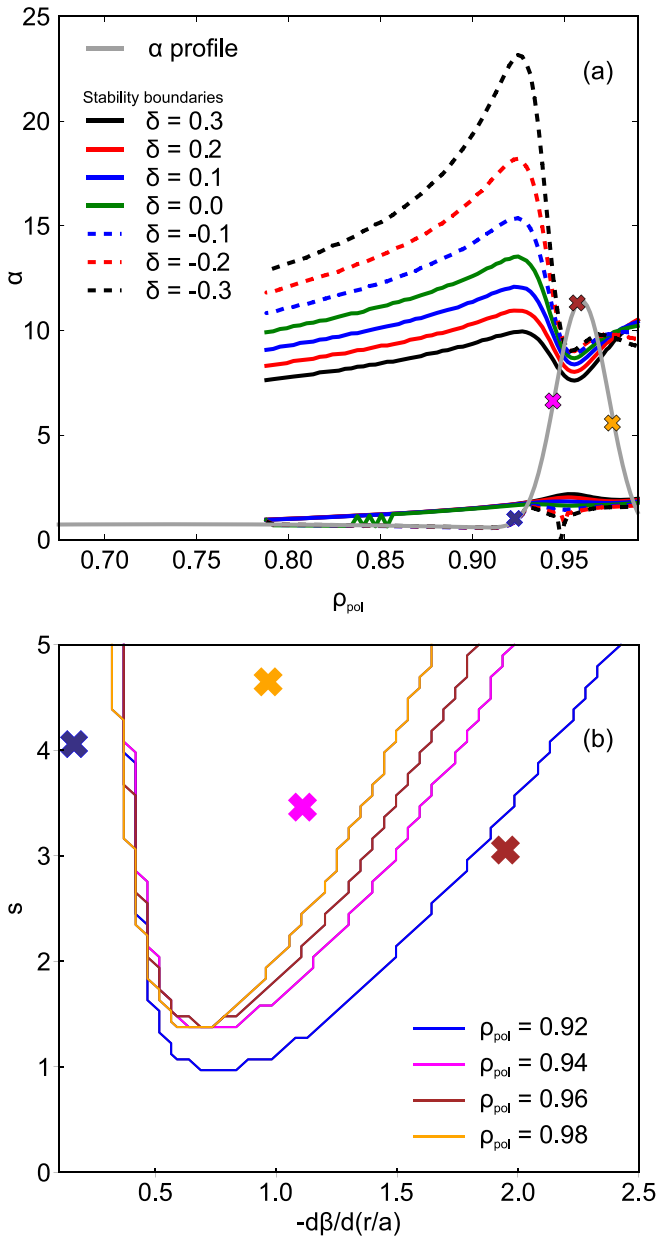

Figure 21. (*a*) α vs $\rho_{\rm pol}$ as calculated by the BALOO code. The α profile in grey corresponds to the p' profile in figure 19, while the colored lines represent the first and second stability boundaries. (*b*) s vs. $-\mathrm{d}\beta/\mathrm{d}(r/a)$ as calculated by the ballstab code for the $\delta = 0.3$ case. The markers show the location of the individual flux surfaces indicated, while the lines represent the stability boundaries, with the left being the first stable region, inside the lines being unstable, and the right the second stable region.

4. Discussion

We analyze here the implications of the simulations presented in the previous sections on both the OBS and NBIHS. At the plasma core, the internal kink and infernal modes are expected to appear in the OBS. We have observed that elevating the q-profile while keeping a flat profile shape leads to an improvement on the stability against these modes. Increasing $\beta_{\rm N}$ has a destabilizing impact on $n = 1, \cdots, 10$ modes. In particular, for $\beta_{\rm N} \sim 4.4$, the internal kink and infernal modes are linearly unstable, and so they are expected to appear in the NBIHS. However, in the experiments, NBI induces a toroidal rotation [61] that, according to our analysis, may have a strong stabilizing effect on infernal modes (through the same physical mechanism by which they can stabilize high-n ballooning modes [62, 63]) if the flow gradient at the mode location is large, whereas they have very little effect on low-n ($n = 1, 2$) modes, probably because of the global character that these modes have. Although there is still no prediction of the expected plasma rotation in SMART, we believe that the toroidal flows will not be enough to stabilize the infernal modes in scenarios with flat q-profiles. We have examined a case (not shown here) with a monotonically increasing q-profile in which $q_0 > 1$ and $\beta_{\rm N} = 3.65$. In such a case, the toroidal flows could not stabilize the infernal modes. Therefore, for the NBIHS with $\beta_{\rm N} \sim 4.4$ and $q_0 < 1$, we should not expect mitigation of infernal modes in the presence of toroidal flows. On the other hand, the exact impact of the toroidal flows on the mode stability, according to our analysis, will depend on the toroidal flow gradient at the mode location. For the $q_0 > 1$ and $\beta_{\rm N} = 3.65$ case, we observed that the impact of the toroidal flows is stronger in PT plasmas than in NT plasmas. The different quantitative impact observed in our simulations is due to the fact that the mode location differs between NT and PT plasmas, which is also modified by the q profile and β.

We have found that the triangularity has a significant impact on the MHD stability of the internal kink and infernal modes found in SMART. In NT plasmas, such modes are more unstable than in PT plasmas, in agreement with other works [64–70]. Nevertheless, we have also observed that toroidal flows might reverse the situation, meaning that NT plasmas could show better MHD stability properties than PT plasmas, assuming the toroidal flow gradient at the mode location is large enough. The SMART experiments should prove the possibility of obtaining such rotation profiles.

Regarding the peeling-ballooning modes, the normalized pressure gradient and current density in the NBIHS are $\alpha_{\rm max} \approx 7$ and $j_{\rm ped}/\langle j \rangle \approx 2.4$, whereas $\alpha_{\rm max} \approx 3.5$ and $j_{\rm ped}/\langle j \rangle \approx 1.6$ in the OBS, respectively. Therefore, peeling-ballooning modes are marginally unstable in the NBIHS with moderate PT, whereas the OBS remains stable against these modes.

According to our simulations, peeling-ballooning modes have a reduced MHD stability boundary in NT-shaped plasmas. The calculations performed with MARS-F help us to understand in which regions of the $(\alpha_{\rm max}, j_{\rm ped}/\langle j \rangle)$ coordinate space peeling-ballooning modes can develop. We may infer from our calculations that NT plasmas might have better consequences for SMART performance compared to PT plasmas, in terms of the peeling-ballooning modes examined here. When the plasma crosses the peeling-ballooning MHD stability boundary, peeling-ballooning modes will develop and saturate, reducing the driving sources, making the plasma bounce back towards the stable region. This means that, in a real experiment, the plasma cannot be found at any arbitrary point of the $(\alpha_{\rm max}, j_{\rm ped}/\langle j \rangle)$ coordinate space. Since in NT configurations we need less $\alpha_{\rm max}$ and $j_{\rm ped}/\langle j \rangle$ to make peeling-ballooning

modes unstable, we would expect less particle and heat transport due to these modes in NT plasmas. The effects of the triangularity on peeling-ballooning modes observed for SMART are consistent with previous modeling works carried out for conventional tokamaks [28, 64, 71, 72].

The MHD instabilities explored here may have detrimental consequences for the performance of projected SMART plasmas. Nonlinear MHD simulations of such cases, carried out with the MHD module of the MEGA code, show that the nonlinear saturation of the internal kink and infernal modes lead to a strong plasma pressure collapse at the plasma core, decreasing the plasma pressure almost by a 50% of its initial value [73]. On the other hand, the plasma edge can be unstable against peeling-ballooning modes at sufficient pressure gradient and current densities, which could eventually drive ELMs. ELMs cause the intermittent relaxation of the edge kinetic profiles, degrading the transport barrier. To ensure high plasma performance, SMART should be equipped with real-time control systems, as they can help to stabilize MHD instabilities and tailor magnetic and kinetic profiles [74–86]. Exploration of natural ELM-free regimes [87], as well as of the recently proposed ELM-free NT edge plasmas [29], should also be pursued. From the modeling side, we have currently designed advanced tokamak MHD equilibria characterized with high reverse shear and very elevated q-profile ($q_0 \sim 5$) and, in the presence of an ideal wall, the MHD stability against $n = 1, 2$ modes significantly improves, allowing to obtain plasmas with $\beta_N \sim 6$ without triggering those modes at the plasma core. Such work will be the focus of a future publication, and will address the coupling of the core modes observed here with external kinks [88]. Another subject left for future work is the vertical stability analysis, which can be of concern with high elongation and significantly changing triangularity as shown in [89].

5. Conclusions

In this paper, we have presented the first MHD stability calculations for the SMART tokamak performed with the MARS-F code. The MHD stability analysis has been carried out for both the plasma core and the plasma edge of SMART.

In the plasma core, we have found that the plasma can be linearly unstable against the internal kink ($n = 1$) and infernal modes ($n = 2, \cdots, 10$). Different parameter scans have been carried out to understand their stability limits. We have seen that the modes are more stable when increasing q, decreasing β_N and increasing δ. The MARS-F simulation results show reasonable agreement with respect to the linear ideal MHD stability analysis with the MHD module of the MEGA code.

The impact that toroidal flows have on the MHD stability of the internal kink and infernal modes has also been addressed. Low-n modes ($n = 1, 2$) become slightly more unstable in the presence of such flows, but the effect is very weak. The $n = 3, \cdots, 10$ infernal modes become more stable in the presence of toroidal flows. The stabilizing impact of the toroidal flows on the infernal modes will depend on the strength of the flow gradient at the corresponding mode location.

The MHD stability of peeling-ballooning modes in the SMART tokamak has been studied in this paper. The simulations indicate that the peeling-ballooning MHD stability boundary is reduced when decreasing the triangularity. The reduced peeling-ballooning MHD stability boundary in NT plasmas could be a path of avoiding the large pressure gradients of the H-mode while keeping a substantial plasma β. In addition, we have checked that a hypothetical conventional SMART tokamak with $A = 3$ has a reduced peeling-ballooning MHD stability boundary in comparison with $A \approx 2$, which is the aspect ratio of the SMART reference scenario [35]. The infinite-n ballooning stability analysis at the plasma edge presented here is consistent with that shown in reference [60].

The impact of the NBI on the MHD stability has been studied in terms of the normalized plasma beta and toroidal rotation in the plasma core, and normalized pressure gradient and current density at the plasma edge. With NBI, the plasma is linearly unstable against the $n = 1$ internal kink and $n = 2, \cdots, 10$ infernal modes, and the toroidal rotation is not expected to fully stabilize the infernal modes; additionally, the peeling-ballooning modes are marginally unstable in PT plasmas with moderate triangularities with NBI. Notice that fast-ion driven modes might appear as a consequence of the NBI, which are out of the scope of this work.

Acknowledgments

This work received funding from the Spanish Ministry of Science (Grant Nos. FPU17/05703 and PID2020-116822RB-I00) and from the European Research Council (ERC) under the European Union's Horizon 2020 research and innovation programme (Grant Agreement No. 805162). This work was supported by the NINS program of Promoting Research by Networking among Institutions. This work was co-funded by the European Regional Development Fund (Andalusian Operational Programme 2014 – 2020) and by the Ministry of Economic Transformation, Industry, Knowledge and Universities of the Junta de Andalucía within the framework of the PAIDI project with reference P18-FR-3812. This work has been carried out within the framework of the EUROfusion Consortium, funded by the European Union via the Euratom Research and Training Programme (Grant Agreement No 101052200 – EUROfusion). Views and opinions expressed are however those of the author(s) only and do not necessarily reflect those of the European Union or the European Commission. Neither the European Union nor the European Commission can be held responsible for them. Additional support was provided by the U.S. Department of Energy under Contract Number DE-ACO2-09CH11466 (PPPL), as well as the Science Undergraduate Laboratory Internship (SULI) program. The authors gratefully acknowledge the computer resources of RES (Spanish

Supercomputing Network) at MareNostrum and the technical support provided by Barcelona Supercomputing Center (BSC), as well as those of CICA (Centro Informático Científico de Andalucía). The authors gratefully acknowledge the help of Oak Nelson with the BALOO code.

ORCID iDs

J. Dominguez-Palacios https://orcid.org/0000-0002-8478-1697
M. Garcia-Munoz https://orcid.org/0000-0002-3241-502X
Y.Q. Liu https://orcid.org/0000-0002-8192-8411
D.J. Cruz-Zabala https://orcid.org/0000-0001-5925-5153
J.W. Berkery https://orcid.org/0000-0002-8062-3210
J. Parisi https://orcid.org/0000-0003-1328-7154
E. Viezzer https://orcid.org/0000-0001-6419-6848
P. Oyola https://orcid.org/0000-0002-8455-1090
S. Futatani https://orcid.org/0000-0001-5742-5454

References

[1] Peng Y.-K.M. and Strickler D.J. 1986 *Nucl. Fusion* **26** 769
[2] Akers R.J. *et al* 2000 *Nucl. Fusion* **40** 1223
[3] Hong B.G. *et al* 2011 *Nucl. Fusion* **51** 113013
[4] Gryaznevich M. *et al* 1998 *Phys. Rev. Lett.* **80** 3972
[5] Gryaznevich M.P. and Sharapov S.E. 2004 *Plasma Phys. Control. Fusion* **46** S15
[6] McClements K.G. *et al* 1999 *Plasma Phys. Control. Fusion* **41** 661
[7] Akers R.J. *et al* 2003 *Plasma Phys. Control. Fusion* **45** A175
[8] Guttenfelder W. and Candy J. 2011 *Phys. Plasmas* **18** 022506
[9] Hofmann F. *et al* 1998 *Phys. Rev. Lett.* **81** 2918
[10] Holcomb C.T. *et al* 2009 *Phys. Plasmas* **16** 056116
[11] Weisen H. *et al* 1997 *Nucl. Fusion* **37** 1741
[12] Moret J.-M. *et al* 1997 *Phys. Rev. Lett.* **79** 2057
[13] Pochelon A. *et al* 1999 *Nucl. Fusion* **39** 1807
[14] Testa D. *et al* 2001 *Nucl. Fusion* **41** 809
[15] Kendl A. and Scott B.D. 2006 *Phys. Plasmas* **13** 012504
[16] Riva F. *et al* 2017 *Plasma Phys. Control. Fusion* **59** 035001
[17] Camenen Y. *et al* 2005 *Plasma Phys. Control. Fusion* **47** 1971
[18] Camenen Y. *et al* 2007 *Nucl. Fusion* **47** 510
[19] Pochelon A. *et al* 2012 *Plasma Fusion Res.* **7** 2502148
[20] Fontana M. *et al* 2018 *Nucl. Fusion* **58** 024002
[21] Huang Z. *et al* 2019 *Plasma Phys. Control. Fusion* **61** 014021
[22] Austin M.E. *et al* 2019 *Phys. Rev. Lett.* **122** 115001
[23] Marinoni A. *et al* 2019 *Phys. Plasmas* **26** 042515
[24] Marinoni A. *et al* 2021 *Nucl. Fusion* **61** 116010
[25] Marinoni A. *et al* 2021 *Rev. Mod. Plasma* **5** 6
[26] Boyes W. *et al* 2023 *Nucl. Fusion* **63** 086007
[27] Paz-Soldan C. *et al* 2024 *Nucl. Fusion* **64** 094002
[28] Happel T. *et al* 2023 *Nucl. Fusion* **63** 016002
[29] Nelson A.O. *et al* 2023 *Phys. Rev. Lett.* **131** 195101
[30] Kikuchi M. *et al* 2019 *Nucl. Fusion* **59** 056017
[31] Agredano-Torres M. *et al* 2021 *Fusion Eng. Des.* **168** 112683
[32] Doyle S.J. *et al* 2021 *Fusion Eng. Des.* **171** 112706
[33] Mancini A. *et al* 2021 *Fusion Eng. Des.* **171** 112542
[34] Podestà M. *et al* 2024 *Plasma Phys. Control. Fusion* **66** 045021
[35] Mancini A. *et al* 2023 *Fusion Eng. Des.* **192** 113833
[36] Pereverzev G.V. *et al* 2002 *IPP Rep.* 5/42 (available at: https://pure.mpg.de/rest/items/item_2138238/component/file_2138237/content)
[37] Cunningham G. 2013 *Fusion Eng. Des.* **88** 3238
[38] Liu Y.Q. *et al* 2000 *Phys. Plasmas* **7** 3681
[39] Troyon F., Gruber R., Saurenmann H., Semenzato S. and Succi S. 1984 *Plasma Phys. Control. Fusion* **26** 209
[40] Troyon F. and Gruber R. 1985 *Phys. Lett.* A **110** 29
[41] Luetjens H. *et al* 1996 *Comput. Phys. Commun.* **97** 219
[42] Von Goeler S. *et al* 1974 *Phys. Rev. Lett.* **33** 1201
[43] Bussac M.N. *et al* 1975 *Phys. Rev. Lett.* **35** 1638
[44] Lang L.L., Liu Y.Q. and Alan D.T. 2021 Magnetic-Confinement Fusion Plasma Theory: Tokamak Magnetohydrodynamic Equilibrium and Stability *Encyclopedia of Nuclear Energy* ed E. Greenspan (Elsevier) pp 431–58
[45] Hastie R.J. and Hender T.C. 1988 *Nucl. Fusion* **28** 585
[46] Charlton L.A. *et al* 1990 *Phys. Fluids* B: *Plasma Phys.* **2** 1574
[47] Zohm H. 2015 *Magnetohydrodynamic Stability of Tokamaks* (Wiley)
[48] Dong G.Q. *et al* 2017 *Phys. Plasmas* **24** 112510
[49] Todo Y. *et al* 1998 *Phys. Plasmas* **5** 1321
[50] Maschke E.K. *et al* 1980 *Plasma Phys.* **22** 579
[51] Iacono R. *et al* 1990 *Phys. Fluids* B **2** 1794
[52] Guazzotto L. *et al* 2005 *Phys. Plasmas* **12** 056107
[53] Poulipoulis G. *et al* 2005 *Phys. Plasmas* **12** 042112
[54] Gryaznevich M.P. *et al* 2008 *Nucl. Fusion* **48** 084003
[55] Snyder P.B. *et al* 2002 *Phys. Plasmas* **9** 2037
[56] Miller R.L. *et al* 1998 *Phys. Plasmas* **5** 973
[57] Knolker M. *et al* 2021 *Nucl. Fusion* **61** 046041
[58] Miller R.L. *et al* 1997 *Phys. Plasmas* **4** 1062
[59] Barnes M. *et al* GS2 v8.1.0 (8.1.0) *Technical Report* Zenodo
[60] Nelson A.O. *et al* 2022 *Nucl. Fusion* **62** 096020
[61] Scott S.D. *et al* 1990 *Phys. Rev. Lett.* **64** 531
[62] Miller R.L. *et al* 1995 *Phys. Plasmas* **2** 3676
[63] Connor J.W. *et al* 2004 *Plasma Phys. Control. Fusion* **46** B1
[64] Medvedev S. *et al* 2015 *Nucl. Fusion* **55** 063013
[65] Ren J. *et al* 2016 *Plasma Phys. Control. Fusion* **58** 115009
[66] Ren J. *et al* 2018 *Nucl. Fusion* **58** 126017
[67] Davies R. *et al* 2022 *Plasma Phys. Control. Fusion* **64** 105001
[68] Liu D. *et al* 2022 *Nucl. Fusion* **62** 112009
[69] Yang X. *et al* 2023 *Nucl. Fusion* **63** 066001
[70] Labbate J.A. *et al* 2023 *In 65th Annual Meeting of the APS Division of Plasma Physics* (*Denver, Colorado, United States*, *30 October– 3 November*)
[71] Merle A. *et al* 2017 *Plasma Phys. Control. Fusion* **59** 104001
[72] Saarelma S. *et al* 2021 *Plasma Phys. Control. Fusion* **63** 105006
[73] Dominguez-Palacios J. *et al* 2023 *7th Asia-Pacific Conf. on Plasma Physics* (*Port Messe Nagoya, Japan*, *12–17 November*) (available at: https://www.aappsdpp.org/DPP2023/html/3contents/topical.html)
[74] Sauter O. *et al* 1997 *Phys. Plasmas* **4** 1654
[75] Chapman I.T. *et al* 2010 *Phys. Rev. Lett.* **105** 255002
[76] Moreau D. *et al* 2011 *Nucl. Fusion* **51** 063009
[77] La Haye R.J. 2006 *Phys. Plasmas* **13** 055501
[78] Gormezano C. *et al* 2007 *Nucl. Fusion* **47** S285
[79] Ou Y. *et al* 2008 *Plasma Phys. Control. Fusion* **50** 115001
[80] Ravensbergen T. *et al* 2021 *Nat. Commun.* **12** 1105
[81] Garrido I. *et al* 2016 *Energies* **9** 609
[82] Valcárcel D.F. *et al* 2010 *Fusion Eng. Des.* **85** 470
[83] Neto A.C. *et al* 2010 *IEEE TNS* **57** 479
[84] Testa D. *et al* 2013 *Plasma Fusion Res.* **9** 1405003
[85] Maingi R. 2014 *Nucl. Fusion* **54** 114016
[86] Liang Y. 2017 *Fusion Sci. Technol.* **59** 586
[87] Viezzer E. 2023 *Nucl. Mater. Energy* **34** 101308
[88] Reyner-Viñolas A. 2024 in preparation
[89] Song J. *et al* 2021 *Nucl. Fusion* **61** 096033